

# Rectification from Radially-Distorted Scales

James Pritts<sup>1</sup>   Zuzana Kukelova<sup>2</sup>   Viktor Larsson<sup>3</sup>   Ondřej Chum<sup>2</sup>

Czech Institute of Robotics, Informatics and Cybernetics (CIIRC), CTU in Prague<sup>1</sup>

Visual Recognition Group (VRG), CTU in Prague<sup>2</sup>

Centre for Mathematical Sciences, Lund University<sup>3</sup>

**Abstract.** This paper introduces the first minimal solvers that jointly estimate lens distortion and affine rectification from repetitions of rigidly transformed coplanar local features. The proposed solvers incorporate lens distortion into the camera model and extend accurate rectification to wide-angle images that contain nearly any type of coplanar repeated content. We demonstrate a principled approach to generating stable minimal solvers by the Gröbner basis method, which is accomplished by sampling feasible monomial bases to maximize numerical stability. Synthetic and real-image experiments confirm that the solvers give accurate rectifications from noisy measurements when used in a RANSAC-based estimator. The proposed solvers demonstrate superior robustness to noise compared to the state-of-the-art. The solvers work on scenes without straight lines and, in general, relax the strong assumptions on scene content made by the state-of-the-art. Accurate rectifications on imagery taken with narrow focal length to near fish-eye lenses demonstrate the wide applicability of the proposed method. The method is fully automated, and the code is publicly available<sup>1</sup>.

## 1 Introduction

This paper proposes minimal solvers that jointly estimate affine rectification and lens distortion from local features extracted from arbitrarily repeating coplanar texture. Wide-angle lenses with significant radial lens distortion are common in consumer cameras like the GoPro series of cameras. In the case of Internet imagery the camera and its metadata are often unavailable for use with off-line calibration techniques. The state-of-the-art has several approaches for rectifying (or partially calibrating) a distorted image, but these methods make restrictive assumptions about scene content by assuming, *e.g.*, the presence of sets of parallel lines [1,2]. The proposed solvers relax the need for special scene structure to unknown repeated structures (see Table 1). The solvers are fast and are robust to noisy feature detections, so they work well in robust estimation frameworks like RANSAC [3]. The proposed work is applicable for several important computer vision tasks including symmetry detection [4], inpainting [5], and single-view 3D reconstruction [6].

The proposed solvers enforce the affine invariant that rectified (and undistorted) repeated regions have the same scale. To allow flexible sampling during robust estimation, we introduce three variants that use different configurations of coplanar repeated regions as input. To model the lens distortion we use the division model proposed by

<sup>1</sup> <https://github.com/prittjam/repeats>



**Fig. 1.** Input (top left image) is a distorted view of a scene plane. The outputs are the undistorted (top right image) and rectified scene planes (bottom row). The method is fully automatic.

Fitzgibbon et al. [7], which is accurate for wide-angle lenses. The use of the division model is critical because other common and effective models result in unsolvable constraint equations (see Sec. 2.1). In addition to the three proposed undistorting solvers, we propose a variant that rectifies under the assumption of a pinhole camera model. The pinhole variant is also a novelty because it does not require a linearization of the rectifying transform in contrast to the state-of-the-art [8,9,10].

The system of polynomial equations encoding the rectifying constraints are solved using an algebraic method based on Gröbner bases. Automated solver-generators using the Gröbner basis method [11,12] were used to generate solvers for several camera geometry estimation problems [11,13,12,14,15]. However, straightforward application of an automated solver-generator to the proposed problem resulted in unstable solvers (see Sec. 5). Recently Larsson et al. [16] sampled feasible monomial bases, which can be used in the action-matrix method. In [16] basis sampling was used to minimize the size of the solver (or the elimination template). We modified the objective of [16] to maximize for the numerical stability of the solvers. The generated solvers with the proposed method are significantly more stable (see Fig. 2), which demonstrates the effectiveness of stability sampling.

Several prior works [8,9,10] assuming the pinhole camera model linearize the rectifying transformation and estimate the local change-of-scale from the Jacobian determinant. The Jacobian determinant is used to induce local constraints on an imaged vanishing line (equivalently, affine-rectification). We attempted to extend the change-of-scale approach by linearizing the undistorting and rectifying transformation, but several difficult problems arose when trying to iterate the parameters to increase the rectification accuracy of the initial estimate (see the supplemental material for further discussion). The complications with the change-of-scale solvers motivated the development of the proposed solvers, which are the first to formulate rectification by encoding the rectified scale of a region directly as a joint function of the measurement region, vanishing line and undistortion parameter.

	Wildenauer et al. [1]	Antunes et al. [2]	Pritts et al. [15]	Proposed
Feature Type	fitted circles	fitted circles	affine-covariant	affine-covariant
Assumption	6 parallel lines	7 parallel lines	1 trans. symmetry	4 repeats
Rectification	multi-model	multi-model	direct	direct

**Table 1.** *Scene Assumptions.* Solvers [1,2] require distinct sets of parallel scene lines as input and multi-model estimation for rectification. Pritts et al. [15] is restricted to scenes with translational symmetries. The proposed solvers can directly rectify from as few as 4 repeats.

There are several related rectification methods that use the fact that lines are distorted by the division model to circles in the image [1,2]. The input to these solvers are circles fitted to extracted contours. Circles that are projections of parallel lines are used to induce constraints on the division model parameter and vanishing point. However, for rectification these methods require distinct sets of imaged parallel lines (6 lines for [1] and 7 for [2]), which is a strong scene content assumption. In order to rectify these methods must solve a multi-model estimation problem to label vanishing points as pair-wise consistent with a vanishing line. In contrast, the proposed solvers can directly undistort and rectify with as few as 4 unknown repeated structures (see Table 1).

Several state-of-the-art methods can compute planar-rectification from imaged repetitions that rigidly transform on the scene planes, but these methods assume a pinhole camera model, which ignores the effect of lens distortion [17,10,5,18]. Pritts et al. [19] attempt to upgrade the pinhole camera model with radial lens distortion by giving an initial guess of scene-plane rectification consistent with a pinhole camera to a non-linear optimization that incorporates a lens-distortion model. However, even with relaxed thresholds, a robust estimator (*i.e.* RANSAC) will discard measurements that capture the most extreme effects of lens distortion, especially around the boundary of the image, since these measurements are not consistent with the pinhole-camera assumption. Thus, failing to account for lens distortion while labeling which measurements to discard as outliers, as done during RANSAC iterations, will give biased fits that underestimate the camera’s lens distortion [14], which in turn degrades rectification accuracy. Pritts et al. [15] were the first to propose minimal solvers that jointly estimate affine rectification and lens distortion, but this method is restricted to scene content with translation symmetries (see Table . Furthermore, we show that the conjugate translation solvers of [15] are significantly more sensitive to noise than the proposed scale-based solvers (see Figs. 2 and 3).

## 2 Problem Formulation

A general homography can be decomposed into an affinity  $H_A$  and projectivity  $H_p$  such that the projective-related parameters are isolated as follows

$$H = H_A H_p = \begin{bmatrix} \mathbf{a}_1^\top \\ \mathbf{a}_2^\top \\ 0 \ 0 \ 1 \end{bmatrix} \begin{bmatrix} 1 & 0 & 0 \\ 0 & 1 & 0 \\ & & \mathbf{h}^\top \end{bmatrix}. \quad (1)$$

Suppose that  $H$  is an *affine-rectifying* homography, which is a homography that transforms the image of the vanishing line  $\mathbf{l} = (l_1, l_2, l_3)^\top$  to the line at infinity  $\mathbf{l}_\infty = (0, 0, 1)^\top$  [20,10]. Thus any homography  $H$  that satisfies the constraint

$$\mathbf{l} = H^\top \mathbf{l}_\infty = \underbrace{H_p^\top H_A^\top}_{\text{from (1)}} (0, 0, 1)^\top = H_p^\top (0, 0, 1)^\top \quad (2)$$

is a rectifying homography. The decomposition of  $H$  by (1) in (2) shows that  $\mathbf{h} = \mathbf{l}$ , and that the affine component of the decomposition of (1) does not move the line at infinity  $\mathbf{l}_\infty$ . From (2), the affine unknowns of  $\mathbf{a}_1^\top$  and  $\mathbf{a}_2^\top$  can be eliminated leaving  $\mathbf{l}$ . The projective component  $H_p$  of an affine-rectifying homography, which is encoded by the image of the vanishing line  $\mathbf{l}$ , is given a special designation  $H_\infty$ ,

$$\alpha_i \mathbf{x}'_i = H_\infty \mathbf{x}_i \quad \text{such that} \quad H_\infty = \begin{bmatrix} 1 & 0 & 0 \\ 0 & 1 & 0 \\ \mathbf{l}^\top \end{bmatrix}, \quad (3)$$

where  $\mathbf{x}'_i$  is a rectified point and  $\alpha$  is nonzero.

## 2.1 Radial Lens Distortion

The rectification equation (3) is valid only if the  $\mathbf{x}_i$  are points from a pinhole camera. Cameras always have some amount of lens distortion. In the case of wide-angle lenses, the non-linear effect can be significant. For lens distorted points, denoted  $\tilde{\mathbf{x}}$ , an undistortion function  $f$  is needed to transform to pinhole points. A common parameterization for radial lens distortion is the one-parameter division model of Fitzgibbon et al. [7], which has the form

$$f(\tilde{\mathbf{x}}_i, \lambda) = (\tilde{x}_i, \tilde{y}_i, 1 + \lambda(\tilde{x}_i^2 + \tilde{y}_i^2))^\top, \quad (4)$$

where the center of distortion is given; i.e.,  $\tilde{\mathbf{x}}_i = (\tilde{x}_i, \tilde{y}_i, 1)$  denotes a center-subtracted measurement from a feature detector. Incorporating the division model into the rectification equation (3) gives

$$\alpha_i \mathbf{x}'_i = (\alpha_i \tilde{x}_i, \alpha_i \tilde{y}_i, \alpha_i)^\top = H_\infty \mathbf{x}_i = H_\infty f(\tilde{\mathbf{x}}_i, \lambda) = (\tilde{x}_i, \tilde{y}_i, l_1 \tilde{x}_i + l_2 \tilde{y}_i + l_3(1 + \lambda(\tilde{x}_i^2 + \tilde{y}_i^2)))^\top. \quad (5)$$

Note that the geometric parameters of interest, namely the division parameter for lens distortion  $\lambda$  and the vanishing line  $\mathbf{l}$  appear only in the homogeneous coordinate  $\alpha_i$ . This fact is leveraged to simplify the solvers derived in the next sections. In fact, we attempted to generate a usable solver for the standard radial distortion polynomial model [20]; however, this model resulted in significantly more complicated equations with 85 solutions and a very large solver.

### 3 Solvers

The proposed solvers use the invariant that rectified coplanar repeats have the same scale. In sections 3.1 and 3.2 we use the constraints induced by the scale invariance of coplanar repeats in rectified space to formulate a system of polynomial equations with the vanishing line and radial distortion parameter as unknowns. Radial lens distortion is modeled with the one-parameter division model from Fitzgibbon et al. [7] as described in Sec. 2.1. The solvers transform coplanar repeat detections to a point-parameterization. The solvers require 3 points from each detected coplanar repeat to measure the scale of the repeat in image space. Oriented affine-covariant regions are used to detect repeats since they encode the necessary geometry for scale estimation. There exists three different minimal cases (see Sec. 3.2) for joint estimation of the vanishing line and division-model parameter. These variants differ by the number of repetitions needed of each repeat. The minimal solvers for the four solver types are constructed in Sec. 3.3. Finally, in Sec. 3.4, we show that equations simplify significantly if the distortion parameter is known, and we are able to construct a much smaller solver for only estimating the rectifying transform.

#### 3.1 Rectified scale constraints from local affine frames

The geometry of an oriented affine-covariant region is given by a local affine frame (LAF). The LAF defines a linear basis at the origin of the oriented affine-covariant region detection. It can be parameterized by the homogeneous transformation  $A_i$ , which defines a change of basis from the right-handed ortho-normal basis to the image space as

$$[\mathbf{x}_{i,1} \ \mathbf{x}_{i,2} \ \mathbf{x}_{i,3}] = A_i \begin{bmatrix} 0 & 0 & 1 \\ 1 & 0 & 0 \\ 1 & 1 & 1 \end{bmatrix}. \quad (6)$$

Thus the LAF  $A_i$  is also minimally parameterized by its *point-parameterization*, which is given by the 3-tuple of homogeneous points  $(\mathbf{x}_{i,1}, \mathbf{x}_{i,2}, \mathbf{x}_{i,3})$ , where  $\mathbf{x}_{i,j} = (x_{i,j}, y_{i,j}, 1)^\top$ .

Suppose that  $\tilde{A}_i$  is the LAF extracted from an oriented affine-covariant region detection imaged by a radially distorted camera. Let  $(\tilde{\mathbf{x}}_{i,1}, \tilde{\mathbf{x}}_{i,2}, \tilde{\mathbf{x}}_{i,3})$  be the point parameterization of the affine frame  $\tilde{A}_i$ . Recall from (5) that  $\alpha_{i,j} \mathbf{x}'_{i,j} = H_\infty f(\tilde{\mathbf{x}}_{i,j}, \lambda)$  undistorts and rectifies where  $\alpha_{i,j} = \mathbf{1}^\top f(\tilde{\mathbf{x}}_{i,j}, \lambda)$ . Then the rectified affine frame in terms of its point parameterization is  $(H_\infty f(\tilde{\mathbf{x}}_{i,1}, \lambda), H_\infty f(\tilde{\mathbf{x}}_{i,2}, \lambda), H_\infty f(\tilde{\mathbf{x}}_{i,3}, \lambda)) = (\alpha_{i,1} \mathbf{x}'_{i,1}, \alpha_{i,2} \mathbf{x}'_{i,2}, \alpha_{i,3} \mathbf{x}'_{i,3})$ , and thus the rectified scale  $s_i$  of  $\tilde{A}_i$  is

$$\begin{aligned} s_i &= \frac{1}{\alpha_{i,1} \alpha_{i,2} \alpha_{i,3}} \cdot \det [\alpha_{i,1} \mathbf{x}'_{i,1} \ \alpha_{i,2} \mathbf{x}'_{i,2} \ \alpha_{i,3} \mathbf{x}'_{i,3}] \\ &= \frac{1}{\alpha_{i,1} \alpha_{i,2} \alpha_{i,3}} \cdot \begin{vmatrix} \tilde{x}_{i,1} & \tilde{x}_{i,2} & \tilde{x}_{i,3} \\ \tilde{y}_{i,1} & \tilde{y}_{i,2} & \tilde{y}_{i,3} \\ \alpha_{i,1} & \alpha_{i,2} & \alpha_{i,3} \end{vmatrix} \\ &= \frac{\alpha_{i,1} \cdot \begin{vmatrix} \tilde{x}_{i,2} & \tilde{x}_{i,3} \\ \tilde{y}_{i,2} & \tilde{y}_{i,3} \end{vmatrix} - \alpha_{i,2} \cdot \begin{vmatrix} \tilde{x}_{i,1} & \tilde{x}_{i,3} \\ \tilde{y}_{i,1} & \tilde{y}_{i,3} \end{vmatrix} + \alpha_{i,3} \cdot \begin{vmatrix} \tilde{x}_{i,1} & \tilde{x}_{i,2} \\ \tilde{y}_{i,1} & \tilde{y}_{i,2} \end{vmatrix}}{\alpha_{i,1} \alpha_{i,2} \alpha_{i,3}} \end{aligned} \quad (7)$$

Note that due to cancellations in the determinant, the numerator in (7) only depends on the distortion parameter  $\lambda$  and  $l_3$ . Rewriting Equation (7) as a constraint on the vanishing line  $\mathbf{l}$  and radial lens distortion parameter  $\lambda$  and rectified scale  $s_i$  gives

$$\sum_{k=1}^3 (-1)^k M_{3,k} \alpha_{i,k} - s_i \prod_{k=1}^3 \alpha_{i,k} = 0, \quad (8)$$

where  $\alpha_{i,j} = \mathbf{l}^\top f(\bar{\mathbf{x}}_{i,j}, \lambda)$  and  $M_{i,j}$  is the  $(i, j)$ -minor of matrix  $[\alpha_{i,1} \mathbf{x}'_{i,1} \alpha_{i,2} \mathbf{x}'_{i,2} \alpha_{i,3} \mathbf{x}'_{i,3}]$ . Note that  $s_i > 0$  since the point parameterization of the affine frame is constructed so that it is right-handed, and that  $M_{3,1}, M_{3,2}, M_{3,3}$  are constant coefficients computed from the point-parameterization of the imaged affine frame  $\hat{\mathbf{A}}_i$ .

### 3.2 Eliminating the rectified scales

The equation (8) gives a constraint between the unknown geometric quantities: (i) division-model parameter  $\lambda$ , (ii) scene-plane vanishing line  $\mathbf{l} = (l_1, l_2, l_3)^\top$ , (iii) and the rectified scale  $s_i$  of image region  $\mathcal{R}_i$ . A unique solution is defined by restricting the vanishing line to the affine subspace  $l_3 = 1$ , which results in degree 4 constraints in unknowns  $\lambda, l_1, l_2$  and  $s_i$ . The alternative of fixing one rectified scale  $s_1$  is rejected since it results in more complicated equations of degree 7.

Let  $\mathcal{R}_i$  and  $\mathcal{R}_j$  be repeated coplanar regions. Then the rectified scales of  $\mathcal{R}_i$  and  $\mathcal{R}_j$  are equal, namely  $s_j = s_i$ . Thus the unknown rectified scales of a group of  $n$  coplanar repeats  $s_1, s_2, \dots, s_n$  can be eliminated in pairs, which gives  $n - 1$  independent constraints and  $\binom{n}{2}$  linearly independent equations.

After eliminating the rectified scales, 3 unknowns remain  $\mathbf{l} = (l_1, l_2, 1)^\top$  and  $\lambda$ , so 3 constraints are needed. There are three minimal configurations: 3 correspondences of 2 coplanar repeats, 1 corresponded set of 3 and 1 correspondence of 2 coplanar repeats, or 1 corresponded set of 4 coplanar repeats. To concisely disambiguate the proposed solvers we introduce denotations for the various correspondence types, which we also use for the state-of-the-art solvers. For example, the solver requiring 1 corresponded set of 3 repeats and a correspondence of 2 repeats is given the prefix  $H_{32}$  and the solvers requiring 2 correspondences of 2 repeats are prefixed by  $H_{22}$ . See Table 2 for all configurations.

The system of equations is of degree 4 regardless of the correspondence type chosen and it has the form

$$\alpha_{j,1} \alpha_{j,2} \alpha_{j,3} \sum_{k=1}^3 (-1)^k M_{3,k} \alpha_{i,k} = \alpha_{i,1} \alpha_{i,2} \alpha_{i,3} \sum_{k=1}^3 (-1)^k M_{3,k} \alpha_{j,k}. \quad (9)$$

For 3 correspondences of 2 coplanar repeats this results in a system of three polynomial equations of degree 4 in three unknowns  $l_1, l_2$  and  $\lambda$ . For 1 corresponded set of 3 and 1 correspondence of 2 coplanar repeats we have 4 equations of degree 4 and for 1 corresponded set of 4 coplanar repeats 6 equations of degree 4. that using all  $\binom{n}{2}$  equations is important for the process of generating solvers and it may lead to smaller solvers. While only 3 equations are necessary, we noticed that for the two latter cases, if not all  $\binom{n}{2}$

equations are used then sometimes spurious solutions are introduced when the rectified scales are eliminated. We also saw that including all equations simplified elimination template construction.

Note that in principal the  $H_{222}$  solver can be used to solve the other cases,  $H_{32}$  and  $H_4$ , as well. However, this essentially decouples the scales within each group of regions, and there will exist additional solutions, which do not satisfy the original constraints.

### 3.3 Creating the solvers

Using the automatic generator from Larsson et al. [12] we created polynomial solvers for the three cases (which we denote  $H_{222}1\lambda$ ,  $H_{32}1\lambda$ , and  $H_41\lambda$ .) The resulting elimination templates were of sizes  $101 \times 155$  (54 solutions),  $107 \times 152$  (45 solutions), and  $115 \times 151$  (36 solutions). The equations involve coefficients of very different magnitude (e.g. both image coordinates  $x_i, y_i \approx 10^3$  and their squares in  $x_i^2 + y_i^2 \approx 10^6$ ). To avoid this problem we rescale both the image coordinates and the squared distances by their average magnitudes. Note that this corresponds to a simple rescaling of the variables in  $(\lambda, l_1, l_2)$ , which is reversed once the solutions are obtained.

Unfortunately, experiments on synthetic data (see Sec. 5.1) revealed that the generated solvers had very poor numerical stability. To find more stable solvers we used the recently proposed basis sampling technique from Larsson et al. [16]. In [16] the authors propose a method for randomly sampling feasible monomial bases which can be used to construct polynomial solvers. Using the heuristic from [16] we generated (with [12]) 1,000 solvers with different monomial bases for the three cases. Following the methodology from Kuang et al. [21], these were then evaluated on a test set of 1,000 synthetic instances and the solvers with the smallest median equation residual were kept. The resulting solvers have slightly larger elimination templates ( $134 \times 187$ ,  $154 \times 199$ , and  $115 \times 151$ ), however they have significantly better numerical stability. See Sec. 5.1 for a comparison between the solvers using the sampled bases and the standard GRevLex bases (default in [12]).

### 3.4 The case of fixed lens distortion

Finally, we also consider the case when the radial lens distortion parameter  $\lambda$  is known. parameters of the vanishing line  $l$ . Fixing  $\lambda$  in (9), the equations become degree 3 in only two unknowns  $l_1$  and  $l_2$ . Since we only have two unknowns, we only need two correspondences. Using again the generator from [12] we find a solver (denoted  $H_{22}l$ ) with an elimination template of size  $12 \times 21$  (9 solutions). In this case it was not necessary to apply the basis sampling.

Note that this solves the affine-rectification problem from two correspondences in closed form. In contrast, the solver from Chum et al. [10] uses a linearization of the scale constraints and may require iterating on the vanishing line estimate to obtain a high-accuracy rectification.

For this setting there is also a second minimal problem for 3 repeated regions having the same rectified scale (so  $H_3$  in the notation above). However, unlike the case for the distortion solvers, this minimal problem turns out to be equivalent to  $H_{22}$ , in the sense

that it also has 9 solutions and can be solved using the  $H_{22}$  solver by simply duplicating one of the regions in the input.

## 4 Robust Estimation

The solvers are used in a LO-RANSAC [22] robust estimation framework. Minimal samples are drawn according to the requirements of the solver (see Table 2) and an affine rectification and lens distortion are estimated. This paper proposes minimal solvers for affine rectification, but metric rectified images are presented in the results for real images. The metric upgrade is directly attempted from the minimal sample (see [19]) and the consensus set is evaluated in the metric rectified space. Models with a maximal consensus set are locally optimized in a method similar to [19].

### 4.1 Features and descriptors

Affine-covariant region detectors are highly repeatable on the same imaged scene texture with respect to significant changes of viewpoint and illumination [23]. Their proven robustness in the multi-view matching task makes them good candidates for representing the local geometry of repeated textures. In particular, for the experiments in Sec. 5 we use the Maximally-Stable Extremal Region and Hessian-Affine detectors [24,25]. The affine covariant regions are given their point parameterization (see Sec. 3.1), equivalently 3 distinct points, which define an affine frame in the image space [26]. The image patch local to the affine frame is embedded into a descriptor vector by the RootSIFT [27,28].

### 4.2 Appearance clustering and Robust Estimation

Affine frames are labeled as repeated texture by their appearance. The appearance of an affine frame is given by the RootSIFT embedding of the image patch local to the affine frame. The RootSIFT descriptors are agglomeratively clustered, which establishes pairwise tentative correspondences among connected components. Each appearance cluster has some proportion of its indices corresponding to affine frames that represent the same repeated scene content, which are the *inliers* of that appearance cluster. The remaining affine frames are the *outliers*.

Samples for the minimal solvers are either 2 correspondences of 2 covariant regions (the  $H_{22}$  solvers), a corresponded set of 3 covariant regions (the  $H_{32}\lambda$  solver) and a correspondence of 2 covariant regions, and a corresponded set of 4 covariant regions (the  $H_4\lambda$  solver). An appearance cluster is selected with probability given by its relative size to the other appearance clusters. The consensus is measured by the number of pairs of affine frames that are mutually consistent with a rigid transform within the appearance group, normalized by the size of each respective group. A non-linear optimizer following [19] is used as the local optimization step.

	$H_2\mathbf{l}u_s\lambda$	$H_{22}\mathbf{l}uvs\lambda$	$H_{22}\mathbf{l}s_i$	$H_{22}\lambda$	$H_{22}\mathbf{l}$	$H_{222}\mathbf{l}\lambda$	$H_{32}\mathbf{l}\lambda$	$H_4\mathbf{l}\lambda$
Reference	[15]	[15]	[10]	[7]				
Rectifies	✓	✓	✓		✓	✓	✓	✓
Undistorts	✓	✓		✓		✓	✓	✓
Motion	trans.	trans.	rigid	rigid*	rigid	rigid	rigid	rigid
# regions	2	4	4	4	4	6	5	4
# sols.	2	4	1	18	9	54	45	36
Size	24x26	76x80	4x4	18x18	12x21	133x187	154x199	115x151

**Table 2.** Proposed (shaded in grey) vs. state-of-the-art solvers. The proposed solvers return more solutions, but most are discarded as complex or infeasible. All correspondences for the  $H_{22}\lambda$  solver must induce the same rigid transform in the scene plane.

## 5 Experiments

The stabilities and noise sensitivities of the proposed solvers are evaluated on synthetic data. We compare the proposed solvers to a bench of 4 state-of-the-art solvers (see Table 2). We apply the denotations for the solvers introduced in Sec. 3 to all solvers in the benchmark. For example, a homography solver requiring 2 corresponded sets, each set containing 2 oriented affine covariant regions begins with the prefix  $H_{22}$ , while, *e.g.*, the proposed solver requiring one corresponded set of 4 oriented affine-covariant regions begins with the prefix  $H_4$ .

Included are two state-of-the-art single-view solvers for radially-distorted conjugate translations, denoted  $H_2\mathbf{l}u_s\lambda$  and  $H_{22}\mathbf{l}uvs\lambda$  [15]; a full-homography and radial distortion solver, denoted  $H_{22}\lambda$  [7]; and the change-of-scale solver for affine rectification of [10], denoted  $H_{22}\mathbf{l}s_i$ . The sensitivity benchmarks measure the performance of rectification accuracy by the warp error (see Sec. 5.1) and the relative error of division parameter estimate. Stability is measured with respect to the estimated division-model parameter. The  $H_{22}\lambda$  solver is omitted from the warp error since the vanishing line cannot be extracted, and the  $H_{22}\mathbf{l}s_i$  and  $H_{22}\mathbf{l}$  solvers are omitted from benchmarks involving lens distortion since the solvers assume a pinhole camera.

### 5.1 Synthetic Data

The performance of the proposed solvers on 1000 synthetic images of 3D scenes with known ground-truth parameters is evaluated. A camera with a random but realistic focal length is randomly oriented and positioned with respect to a 10x10 square meter scene plane such that the plane is mostly in the camera’s field-of-view. The image resolution is set to 1000x1000 pixels. Conjugately translated affine frames are generated on the scene plane such that their scale with respect to the scene plane is realistic. The motion is restricted to conjugate translations so that [15] can be included in the benchmark. See the extended experiments in the supplemental for the same study on corresponded sets of rigidly transformed affine frames. The modeling choice reflects the use of affine-covariant region detectors on real images. The conjugately translated regions are distorted according to the division model, and, for the sensitivity experiments, isotropic

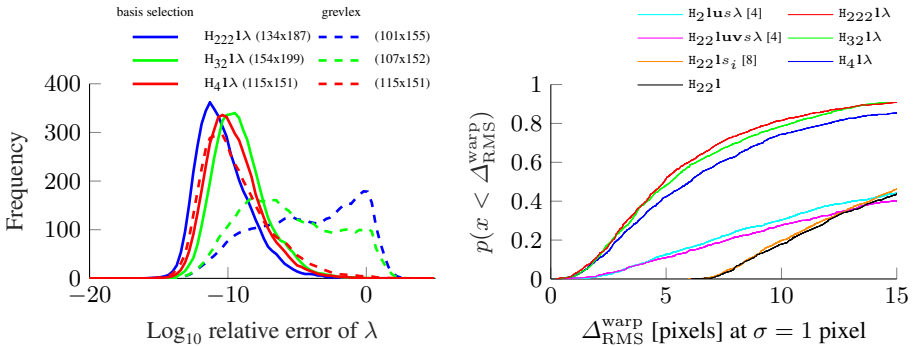


**Fig. 2.** *Stability study* (left): shows that the basis selection method of [16] is essential for stable solver generation. *Proposal study* (right): reports the cumulative distributions of raw warp errors (see Sec. 5.1) for the bench of solvers on 1000 synthetic scenes 1- $\sigma$  pixel of imaging white noise. The proposed solvers (with distortion) give significantly better proposals than the state-of-the-art.

white noise is added to the distorted affine frames at increasing levels. Performance is characterized by the relative error of the estimated distortion parameter and by the warp error, which measures the accuracy of the undistortion and rectification.

**Warp error** Since the accuracy of scene-plane rectification is a primary concern, the warp error for rectifying homographies proposed by Pritts et al. [29] is reported, which we extend to incorporate the division model for radial lens distortion. A round trip between the image space and rectified space is made by undistorting and rectifying imaged coplanar points by the estimated lens distortion  $\hat{\lambda}$  and rectifying homography  $\hat{H}_\infty$  and then re-warping and distorting the rectified points into the image by a synthetic camera constructed from the ground-truth lens distortion  $\lambda$  and rectifying homography  $H_\infty$ . Ideally, the synthetic camera constructed from the truth would project the undistorted and rectified points onto the original points. The scene plane is tessellated by a 10x10 square grid of points  $\{\mathbf{X}_i\}$  and imaged as  $\{\tilde{\mathbf{x}}_i\}$  by the ground-truth camera. The tessellation ensures that the warp error is measure uniformly over the entire scene plane.

Note that there is an affine ambiguity, denoted  $A$ , between  $\hat{H}_\infty$  and  $H_\infty$ , which is folded into the expression for the synthetic camera, namely  $P(A) = (A H_\infty)^{-1}$ , and estimated during computation of the warp error,

$$\Delta^{\text{warp}} = \min_{\hat{A}} \sum_i d^2(\tilde{\mathbf{x}}_i, f^d(P(\hat{A})\hat{H}_\infty f(\tilde{\mathbf{x}}_i, \hat{\lambda})), \hat{\lambda}), \quad (10)$$

where  $d(\cdot, \cdot)$  is the Euclidean distance, and  $\{\tilde{\mathbf{x}}_i\}$  are the imaged grid points of the scene-plane tessellation. The root mean square error for  $\{\tilde{\mathbf{x}}_i\}$  is reported and denoted as  $\Delta_{\text{RMS}}^{\text{warp}}$ . Note that the vanishing line is not directly estimated by the solver  $H_{22}\lambda$  of [7], so it is not reported.

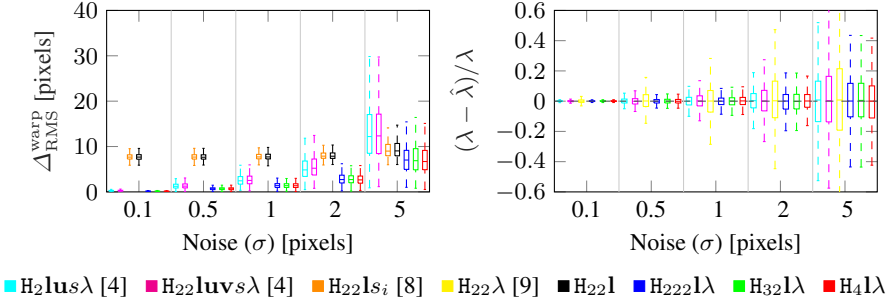


**Fig. 3.** *Sensitivity benchmark.* Comparison of two error measures after 25 iterations of a simple RANSAC for different solvers with increasing levels of white noise added to the affine correspondences. (left) reports the warp error as  $\Delta_{\text{RMS}}^{\text{warp}}$  and (right) reports the relative error of the estimated division model parameter. The proposed solvers show significantly better robustness to noise.

**Numerical Stability** The stability study measures the relative error of the estimated division model parameter for the solver benchmark for noiseless affine-frame correspondences across realistic scene and camera configurations, which are generated as described in the introduction to Sec. 5.1. The ground-truth parameter of the division model  $\lambda$  is drawn uniformly at random from the interval  $[-8, 0.5]$ . For a reference, the division parameter of  $\lambda = -4$  is typical for wide field-of-view cameras like the GoPro, where the image is normalized by  $\frac{1}{\text{width}+\text{height}}$ . Fig. 2 (left) reports the histogram of  $\log_{10}$  relative error of the estimates of the division model parameter.

The stability study compares the two approaches for creating the solvers described in Sec. 3.3, denoted *grexlex* and *basis selection* in the figure. The automatic solver generator of Larsson et al. [12] et al. was used to generate both sets of solvers. Fig. 2 shows that basis selection method of [16] significantly improves the stability of the generated solvers. The basis-sampled solvers are used going forward for the remainder of the experiments.

**Noise Sensitivity** The proposed and state-of-the-art solvers are tested with increasing levels of white noise added to the point parameterizations (see Sec.3.1) of imaged oriented affine-covariant region correspondences, which are relatively oriented and positioned to each other by translations in the scene plane (equivalently conjugate translations, see [15,30]). The white noise is parameterized by the standard-deviation of a zero-mean isotropic Gaussian distribution, and the solvers are tested at noise levels of  $\sigma \in \{0.1, 0.5, 1, 2, 5\}$ . The ground-truth division model parameter is set to  $\lambda = -4$ , which is typical for GoPro-type imagery.

The proposal study in the right panel of Fig. 2 shows that for 1-pixel white noise, the proposed 8solvers— $H_{222}l\lambda$ ,  $H_{32}l\lambda$  and  $H_4l\lambda$ —give significantly more accurate estimates than the state-of-the-art conjugate translation solvers of [15]. If 5 pixel RMS warp error is fixed as threshold for a good model proposal, then half of the models given by the proposed solvers are good verses less than 20% by [15]. The input to the conjugate

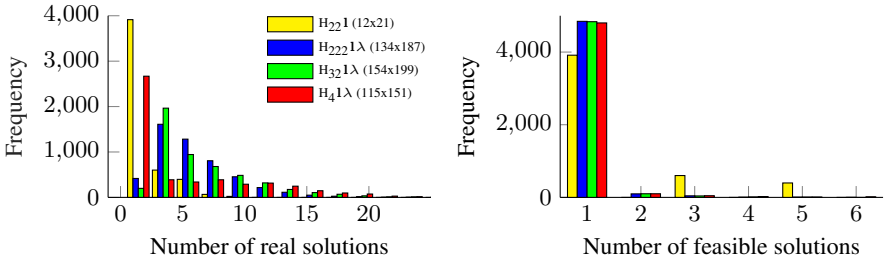


**Fig. 4.** *Real and feasible solutions.* (left) The histogram of real solutions for the proposed solvers. (right) There is typically only 1 feasible real solution.

translation solvers are the point-parameterizations of the affine correspondences, which are far more sensitive to noise than the measured area of the affine correspondences, which is used by the proposed solvers. The proposed  $H_{22}l$  solver and  $H_{22}ls_i$  [10] both give biased proposals since they don’t estimate lens distortion.

For Fig. 3 the solvers are wrapped in a simple RANSAC-loop, which minimizes the RMS warp error  $\Delta_{\text{RMS}}^{\text{warp}}$  over 25 corresponded sets of affine frames. Results are calculated from the optimal estimate given by RANSAC as measured by the warp error and summarized for 1000 generated scenes as boxplots. The interquartile range is contained within the extents of a box, and the median is the horizontal line dividing the box. As shown in Fig. 3, the proposed solvers— $H_{222}l\lambda$ ,  $H_{32}l\lambda$  and  $H_4l\lambda$ —give the most accurate lens distortion and rectification estimates. The solvers are competitive or superior to the state-of-the-art at the 0.5 pixel noise level. The change-of-scale solver  $H_{22}ls_i$  of [10] shows significant bias since it assumes a pinhole camera model. We don’t report  $H_{22}l$  since it has the same noise characteristic as  $H_{22}ls_i$ , see Fig. 2 (right). All of the proposed solvers estimating distortion give a solution with less than 5 pixel RMS warp error  $\Delta_{\text{RMS}}^{\text{warp}}$  and estimate the correct division model parameter more than half the time at the 2 pixel noise level with 25 iterations of RANSAC. This suggests that the proposed solvers are good candidates for a robust undistortion and rectification framework.

**Real and feasible solutions** Fig. 4 (left) shows the number of real solutions for 5000 synthetic instances, and Fig. 4 (right) shows the number of feasible solutions, i.e. when the distortion parameter was in the interval  $[-8, 0.5]$  (for the  $H_{22}l$  solver each real solution was considered feasible). While the proposed minimal problems have a lot of solutions (see Table 2), we can see in Fig. 4 that we in general only have to do further validation on a very small subset of the solutions.

**Runtime** The runtime of the solvers, implemented in MATLAB and on a standard desktop computer, are 2 ms ( $H_{222}l\lambda$ ), 2.2 ms ( $H_{32}l\lambda$ ), 1.7 ms ( $H_4l\lambda$ ) and 0.2 ms ( $H_{22}l$ ). Since solvers with distortion have a large number of solutions, it is reasonable to expect that the solvers could be sped up significantly by replacing the large eigenvalue computations with Sturm sequences [31] and searching only for eigenvalues in some feasible interval. Usually (97% of cases in experiments) only a single solution is feasible.

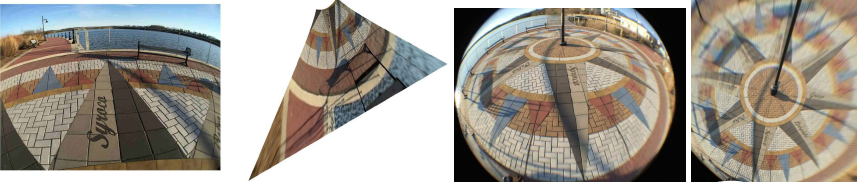


**Fig. 5.** (left pair) The waterfront and fence appear to be distorted scene lines, but they are on the circumference of a compass. (right pair) The scene is imaged by a fish-eye lens, and a reasonable rectification is estimated with proposed method.

## 5.2 Real Images

The field-of-view experiment tests the proposed solvers on real images taken with lenses sampled along the spectrum of fields of view: narrow, medium, wide and fisheye. As a general rule, radial distortion increases with the field-of-view. The imagery was selected to have challenging and diverse content. Fig.6 shows highly accurate rectification by the  $H_{222}1\lambda$  solver for images with increasing amounts of radial distortion. More imagery can be found in the supplementary material.

The solver-comparison benchmark (Fig.7) compares the proposed  $H_{222}1\lambda$  and  $H_{22}1$  solvers to the state-of-the-art solvers on images that contain scene planes with either translated or rigidly transformed repeated patterns. For radially distorted images with rigidly transformed repeated patterns, the proposed  $H_{222}1\lambda$  solver was the only solver capable of accurately rectifying scene planes. Across all image types the  $H_{222}1\lambda$  solver gave the best rectifications. Also noteworthy is the  $H_{22}1$  solver, which gave rectifications as least as good as the change-of-scale solver of Chum et al. [10].

Fig. 5 presents a deceiving landmark imaged by a wide-angle and fisheye lens. From the wide-angle image, it is not obvious which lines are really straight in the scene, and an attempt to undistort this image by using the plumbline constraint would likely fail.

## 6 Conclusion

This paper proposes solvers that extend affine-rectification to radially-distorted images that contain essentially arbitrarily repeating coplanar patterns. Synthetic experiments demonstrate that the proposed solvers are less sensitive to noise with respect to the state-of-the-art while being applicable to a broader set of image content. The paper demonstrates that robust solvers can be consistently generated with basis selection [16] by maximizing for numerical stability. Experiments on difficult real imagery with large amounts of radial distortion confirm that the solvers give high-accuracy rectifications when used inside a robust estimator. By jointly estimating rectification and radial distortion, the proposed minimal solvers eliminate the need for sampling lens distortion parameters during RANSAC.

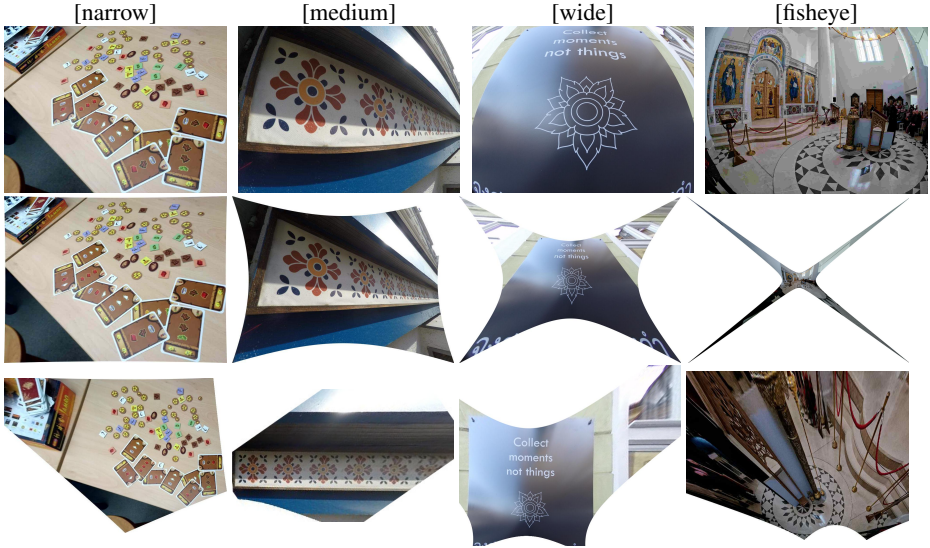


**Fig. 6.** *Field-of-View Study.* Images are sampled (left-to-right) along the field-of-view continuum: Android phone, GoPro Hero 4 at the medium and wide FOV settings, Panasonic DMC-GM5 w. a Samyang 7.5mm fisheye lens. (middle row) Undistorted images (bottom row) rectified results.

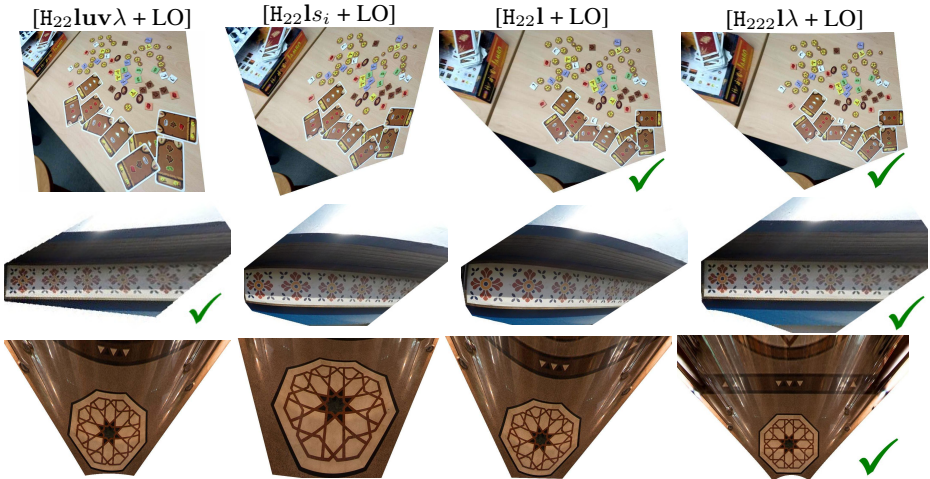


**Fig. 7.** *Solver comparison.* Images are categorized by the distortion amount and pattern configuration: (top) small distortion w. general motion, (middle) medium distortion w. translation (bottom) large distortion w. general motion.

## References

1. Wildenauer, H., Micusík, B.: Closed form solution for radial distortion estimation from a single vanishing point. In: *BMVC*. (2013)
2. Antunes, M., Barreto, J.P., Aouada, D., Ottersten, B.: Unsupervised vanishing point detection and camera calibration from a single manhattan image with radial distortion. In: *CVPR*. (2017)
3. Fischler, M.A., Bolles, R.C.: Random sample consensus: A paradigm for model fitting with applications to image analysis and automated cartography. *CACM* **24** (1981) 381–395
4. Funk, C., Lee, S., Oswald, M.R., Tsogkas, S., Shen, W., Cohen, A., Dickinson, S., Y., L.: 2017 iccv challenge: Detecting symmetry in the wild. In: *ICCV Workshop*. (2017)
5. Lukáč, M., Sýkora, D., Sunkavalli, K., Shechtman, E., Jamriška, O., Carr, N., Pajdla, T.: Nautilus: Recovering regional symmetry transformations for image editing. *ACM Trans. Graph.* **36** (2017) 108:1–108:11
6. Wu, C., Frahm, J.M., Pollefeys, M.: Repetition-based dense single-view reconstruction. In: *CVPR*. (2011)
7. Fitzgibbon, A.W.: Simultaneous linear estimation of multiple view geometry and lens distortion. In: *CVPR*. (2001)
8. Ohta, T., Maenobu, K., Sakai, T.: Obtaining surface orientation from texels under perspective projection. In: *IJCAI*. (1981)
9. Criminisi, A., Zisserman, A.: Shape from texture: homogeneity revisited. In: *BMVC*. (2000)
10. Chum, O., Matas, J.: Planar affine rectification from change of scale. In: *ACCV*. (2010)
11. Kukulova, Z., Bujnak, M., Pajdla, T.: Automatic generator of minimal problem solvers. In: *ECCV*. (2008)
12. Larsson, V., Åström, K., Oskarsson, M.: Efficient solvers for minimal problems by syzygy-based reduction. In: *CVPR*. (2017)
13. Larsson, V., Åström, K., Oskarsson, M.: Polynomial solvers for saturated ideals. In: *ICCV*. (2017)
14. Kukulova, Z., Heller, J., M., B., Pajdla, T.: Radial distortion homography. In: *CVPR*. (2015)
15. Pritts, J., Kukulova, Z., Larsson, V., Chum, O.: Radially-distorted conjugate translations. In: *CVPR*. (2018)
16. Larsson, V., Oskarsson, M., Åström, K., Wallis, A., Kukulova, Z., Pajdla, T.: Beyond gröbner bases: Basis selection for minimal solvers. *CoRR* **abs/1803.04360** (2018)
17. Aiger, D., Cohen-Or, D., Mitra, N.: Repetition maximization based texture rectification. *Computer Graphics Forum* **31** (2012) 439–448
18. Zhang, Z., Ganesh, A., Liang, X., Ma, Y.: TILT: transform invariant low-rank textures. *IJCV* **99** (2012) 1–24
19. Pritts, J., Chum, O., Matas, J.: Detection, rectification and segmentation of coplanar repeated patterns. In: *CVPR*. (2014)
20. Hartley, R.I., Zisserman, A.W.: *Multiple View Geometry in Computer Vision*. Second edn. Cambridge University Press, ISBN: 0521540518 (2004)
21. Kuang, Y., Åström, K.: Numerically stable optimization of polynomial solvers for minimal problems. In: *ECCV*. (2012)
22. Chum, O., Matas, J., Obdržálek, v.: Enhancing RANSAC by generalized model optimization. In: *ACCV*. (2004)
23. Mikolajczyk, K., Schmid, C.: A performance evaluation of local descriptors. *PAMI* (2004)
24. Matas, J., Chum, O., Urban, M., Pajdla, T.: Robust wide baseline stereo from maximally stable extremal regions. In: *BMVC*. (2002)
25. Mikolajczyk, K., Schmid, C.: Scale and affine invariant interest point detectors. Volume 60. (2004)

26. Obdržálek, Š., Matas, J.: Object recognition using local affine frames on distinguished regions. In: BMVC. (2002)
27. Arandjelović, R., Zisserman, A.: Three things everyone should know to improve object retrieval. In: CVPR. (2012)
28. Lowe, D.: Distinctive image features from scale-invariant keypoints. *IJCV* **60** (2004) 91–110
29. Pritts, J., Rozumnyi, D., Kumar, M.P., Chum, O.: Coplanar repeats by energy minimization. In: BMVC. (2016)
30. Schaffalitzky, F., Zisserman, A.: Geometric grouping of repeated elements within images. In: BMVC. (1998)
31. Bujnak, M., Kukelova, Z., Pajdla, T.: Making minimal solvers fast. In: CVPR. (2012)
32. Barath, D., Hajder, L.: A theory of point-wise homography estimation. *Pattern Recognition Letters* **94** (2017) 7 – 14
33. Köser, K., Beder, C., Koch, R.: Conjugate rotation: Parameterization and estimation from an affine feature correspondence. In: CVPR. (2008)
34. Köser, K., Koch, R.: Differential spatial resection - pose estimation using a single local image feature. In: ECCV. (2008)

## A Change of scale solver

In the introduction it was mentioned that Chum et al. and Ohta et al. [8,10] proposed solvers that used the Jacobian determinant of the rectifying transformation to induce local constraints on the imaged vanishing line. The Jacobian determinant gives the change-of-scale of a function at a point, which motivates the name for this type of solver. In this section we propose an extension of Chum et al. [10], which linearizes the undistorting and rectifying function defined below in (11).

The change-of-scale solver uses local constraints induced on the Jacobian of the undistorting and rectifying function to solve for the vanishing line and distortion parameter. There are several related works that linearize the homography and use constraints on the Jacobian [32,10,8,33,34]; however, the proposed change-of-scale solver is the first solver to incorporate lens distortion with this approach. In particular, we provide the derivation of a solver for the division model for radial lens distortion [7], which leverages the fact that the unknown division model parameter is encoded exclusively in the homogeneous coordinate (see (3)). The change-of-scale solver has the advantage that it works for any scale-covariant region detector.

The Euclidean coordinates of the rectified point  $\mathbf{x}'$ —the inhomogeneous representation of  $\mathbf{x}'_i = H_{\infty} f(\tilde{\mathbf{x}}_i, \lambda)$  (refer to (5))—of any imaged point  $\tilde{\mathbf{x}}_i = (\tilde{x}_i, \tilde{y}_i, 1)^\top$  on the scene plane is given by the vector-valued nonlinear function

$$\mathbf{x}'(\tilde{x}, \tilde{y}) = (x(\tilde{x}, \tilde{y}), y(\tilde{x}, \tilde{y}))^\top = \left( \frac{\tilde{x}}{\Gamma^1 f(\tilde{\mathbf{x}}, \lambda)}, \frac{\tilde{y}}{\Gamma^1 f(\tilde{\mathbf{x}}, \lambda)} \right)^\top. \quad (11)$$

The function  $\mathbf{x}'$  is linearized about the point  $(\tilde{x}, \tilde{y})$  with the first-order Taylor expansion,

$$\mathbf{x}'(\tilde{x} + \delta_{\tilde{x}}, \tilde{y} + \delta_{\tilde{y}}) = \mathbf{x}'(\tilde{x}, \tilde{y}) + \mathbf{J}_{\mathbf{x}'}(\mathbf{1}, \lambda)|_{(\tilde{x}, \tilde{y})} \cdot (\delta_{\tilde{x}}, \delta_{\tilde{y}})^\top. \quad (12)$$

The Jacobian determinant  $\det(\mathbf{J}_{\mathbf{x}'}(\mathbf{1}, \lambda)|_{(\tilde{x}_i, \tilde{y}_i)})$  gives the approximate change of scale, of the rectifying and undistorting function  $\mathbf{x}'$  near the point  $(\tilde{x}, \tilde{y})^\top$ . Let  $\tilde{s}_i$  be the scale of an image region  $\mathcal{R}_i$  with its centroid at  $(\tilde{x}_i, \tilde{y}_i)^\top$ , where the preimage of  $\mathcal{R}_i$  is on some scene plane  $\pi$ . Let  $s_i$  be the rectified scale of  $\mathcal{R}_i$ . Then  $\tilde{s}_i$  can be expressed in terms of the unknown rectified scale  $s_i$  and the Jacobian determinant as

$$\tilde{s}_i = \det(\mathbf{J}_{\mathbf{x}'}^{-1}(\mathbf{1}, \lambda)|_{(\tilde{x}_i, \tilde{y}_i)}) \cdot s_i = \det(\mathbf{J}_{\mathbf{x}'}(\mathbf{1}, \lambda)|_{(\tilde{x}_i, \tilde{y}_i)})^{-1} \cdot s_i \quad (13)$$

### A.1 Eliminating the rectified scale

The constraint equation in (13) defines the unknown geometric quantities: (i) division-model parameter  $\lambda$ , (ii) scene-plane vanishing line  $\mathbf{l} = (l_1, l_2, l_3)^\top$ , (iii) and the rectified scale  $s_i$  of image region  $\mathcal{R}_i$ . The imaged region scale  $\mathcal{R}_i$  is measured by some scale-covariant region detector, *e.g.*, the SIFT or Hessian Affine detector [28,25]. A unique solution is defined by restricting the vanishing line to the affine subspace  $l_3 = 1$ , which results in degree 4 constraints. The alternative of fixing the rectified scale  $s_i$  is rejected since it results in higher degree constraints. Let  $\mathcal{R}_i$  and  $\mathcal{R}_j$  be repeated coplanar regions. Then the rectified scales of  $\mathcal{R}_i$  and  $\mathcal{R}_j$  are equal, namely  $s_j = s_i$ . Thus the unknown rectified scales of a group of  $n$  co-planar repeats  $s_1, s_2, \dots, s_n$  can be eliminated in pairs, which gives  $n - 1$  constraints and  $\binom{n}{2}$  linearly independent equations.



**Fig. A.1.** *Change-of-scale solver.* (top row) Input images (bottom row) Undistorted and rectified results using the initial estimate from the change-of-scale solver. The undistortion and projective warp are undercorrected.

## A.2 Creating the solver

After eliminating the rectified scales, 3 unknowns remain  $\mathbf{l} = (l_1, l_2, 1)^\top$  and  $\lambda$ , so 3 equations are needed. The minimal configurations can be obtained from 3 correspondences of 2 coplanar repeats, 1 corresponded set of 3 and 1 correspondence of 2 coplanar repeats, or 1 corresponded set of 4 coplanar repeats. The system of equations contains rational equations of the form

$$\tilde{s}_i \cdot \det(\mathbf{J}_{\mathbf{x}'}(\mathbf{l}, \lambda)|_{(\tilde{x}_j, \tilde{y}_j)}) = \tilde{s}_j \cdot \det(\mathbf{J}_{\mathbf{x}'}(\mathbf{l}, \lambda)|_{(\tilde{x}_i, \tilde{y}_i)}). \quad (14)$$

After multiplying equations (14) by common denominators we obtain a system of three quartic polynomial equations in three unknowns, namely  $l_1, l_2$  and  $\lambda$ . We used the automatic generator from Larsson et al. [12] to create the polynomial solver variant taking an input of 3 correspondences of 2 coplanar repeats was generated. The structure of the change-of-scale solver for this correspondence configuration is the same as the  $H_{2222}\lambda$  solver (*i.e.*, same monomials, but the coefficients are computed differently), so there exists 54 solutions for the change-of-scale solver as well. The feasibility of the change-of-scale formulation with for lens-distortion and rectification estimation was evaluated with this solver.

## A.3 Challenges with refining the estimate

The proposed change-of-scale solver assumes that  $\det(\mathbf{J}(\mathbf{l}, \lambda)|_{(\tilde{x}_i, \tilde{y}_i)})$ , where  $(\tilde{x}_i, \tilde{y}_i)^\top$  is the centroid of imaged region  $\mathcal{R}_i$ , is exact over the entirety of the imaged region  $\mathcal{R}_i$ . In fact, it is only exact for infinitesimally small regions. To reduce the linearization error for rectifying transformations, Chum et al. [10] proposed an iterative scheme:

1. let  $\mathcal{I}^{(0)}$  be the original image
2. estimate the vanishing line  $\hat{\mathbf{l}}^{(t)}$  for the current iteration  $t$  for image  $\mathcal{I}^{(t-1)}$
3. calculate the rectified image  $\mathcal{I}^{(t)}$  from  $\mathcal{I}^{(t-1)}$  by using  $\hat{\mathbf{l}}^{(t)}$  to construct  $\hat{\mathbf{H}}_{\infty}^{(t)}$ .
4. if  $\hat{\mathbf{H}}_{\infty}^{(t)} \approx \mathbf{I}_3$  then goto step 5, else goto step 2.
5. let  $\hat{\mathbf{H}}_{\infty} = \prod_{t=1}^N \hat{\mathbf{H}}_{\infty}^{(t)}$ , where  $N$  is the number of iterations.

The perspective distortion from imaging at  $\mathcal{I}^{(t)}$  is less than that of  $\mathcal{I}^{(0)}$ , so the linearized rectifying transform is better approximation in the space of  $\mathcal{I}^{(t)}$ . However, Chum et al. offer no proof that this scheme converges, and, in practice, the linearization for a strictly rectifying transformation is good enough to use directly [10].

In contrast, the initial estimates from the proposed solver of  $\hat{\lambda}^{(0)}$  and  $\hat{\mathbf{l}}^{(0)}$  are an under-correction of the radial lens distortion and perspective distortion (see Fig. A.1). Furthermore, the algorithm defined above cannot be directly applied. The operations of undistortion and rectification do not commute. In other words, rectification must be applied to a pinhole camera. We experimented with keeping only the lens distortion parameter estimates to construct a pinhole camera, but these results were not satisfactory.

The complications with parameter refinement motivated the development of the non-iterative solver. The development of a well-posed iterative scheme is left for future work.

## B Using reflections

In the derivation of constraints for the  $\mathbf{H}_{222}\mathbf{l}\lambda$ ,  $\mathbf{H}_{32}\mathbf{l}\lambda$  and  $\mathbf{H}_4\mathbf{l}\lambda$  solvers, the rectified scales  $s_i$  of the corresponded affine-covariant regions were set equal to each other so that they could be eliminated from the unknowns (see Sec. 3.3). Note that the rectified scale  $s_i$  in (7) is signed, which seems to preclude using reflected affine-covariant regions, *i.e.*, jointly using left-handed and right-handed point-parameterizations in the measurements. In fact, the sign of the scale is irrelevant and the magnitude is the measurement used to enforce the affine invariant that coplanar repeats must have the same scale in a rectified space. Using absolute value is not possible in (7) since the resulting constraints would not be polynomial equations, and squaring the rectified scale is also not possible since the resulting constraint equations would be intractable. But a simple preprocessing trick admits the use of mixed left and right-handed point-parameterization of affine-covariant regions. Suppose that  $\det [\tilde{\mathbf{x}}_{i,1} \tilde{\mathbf{x}}_{i,2} \tilde{\mathbf{x}}_{i,3}] < 0$ , where  $(\tilde{\mathbf{x}}_{i,1}, \tilde{\mathbf{x}}_{i,2}, \tilde{\mathbf{x}}_{i,3})$  is a distorted left-handed point parameterization of an affine-covariant region. Then reordering the point parameterization as  $(\tilde{\mathbf{x}}_{i,3}, \tilde{\mathbf{x}}_{i,2}, \tilde{\mathbf{x}}_{i,1})$  results in a right-handed point-parameterization such that  $\det [\tilde{\mathbf{x}}_{i,3} \tilde{\mathbf{x}}_{i,2} \tilde{\mathbf{x}}_{i,1}] > 0$ , and the absolute magnitude of its rectified scale remains the same. This reordering allows the mixing of handedness in the measurements.

## C Extended experiments

The extended experiments in the following pages include (i) noise sensitivity experiments that report the raw relative estimation error and warp error for conjugate translations (*i.e.*, results without RANSAC as reported in Fig. 3 can be found in Fig. C.1).

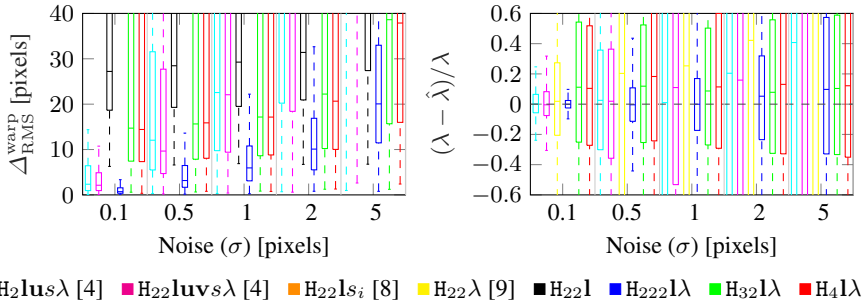


**Fig. C.1.** *Conjugately translated coplanar repeats raw sensitivity benchmark.* Raw comparison of the benchmark solvers (results of the solvers without RANSAC) for increasing levels of white noise added to the point parameterizations of the oriented affine-covariant regions. (left) reports the warp error as  $\Delta_{\text{RMS}}^{\text{warp}}$  and (right) reports the relative radial lens distortion error.

(ii) noise sensitivity experiments for coplanar repeats that are rigidly transformed in the scene plane (see Fig. C.2), (iii) and the undistortion and metric rectification of images for various wide-angle lenses, which further demonstrates the proposed solver’s effectiveness on diverse image content.

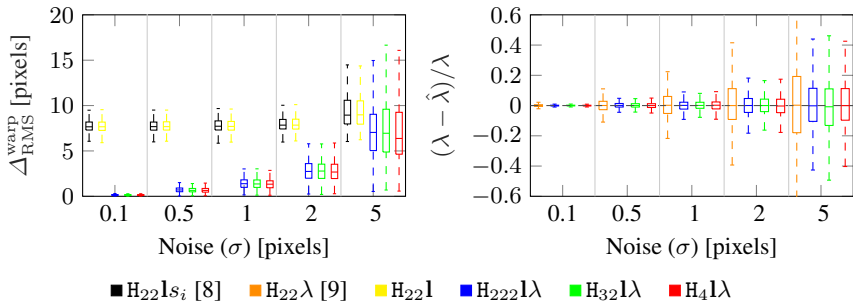


**Fig. C.2.** *Rigidly transformed coplanar repeats RANSAC sensitivity benchmark.* Comparison of the benchmark solvers after 25 iterations of a simple RANSAC for different solvers with increasing levels of white noise added to the point parameterizations of the oriented affine-covariant regions. (left) reports the warp error as  $\Delta_{\text{RMS}}^{\text{warp}}$  and (right) reports the estimated radial lens distortion relative error.

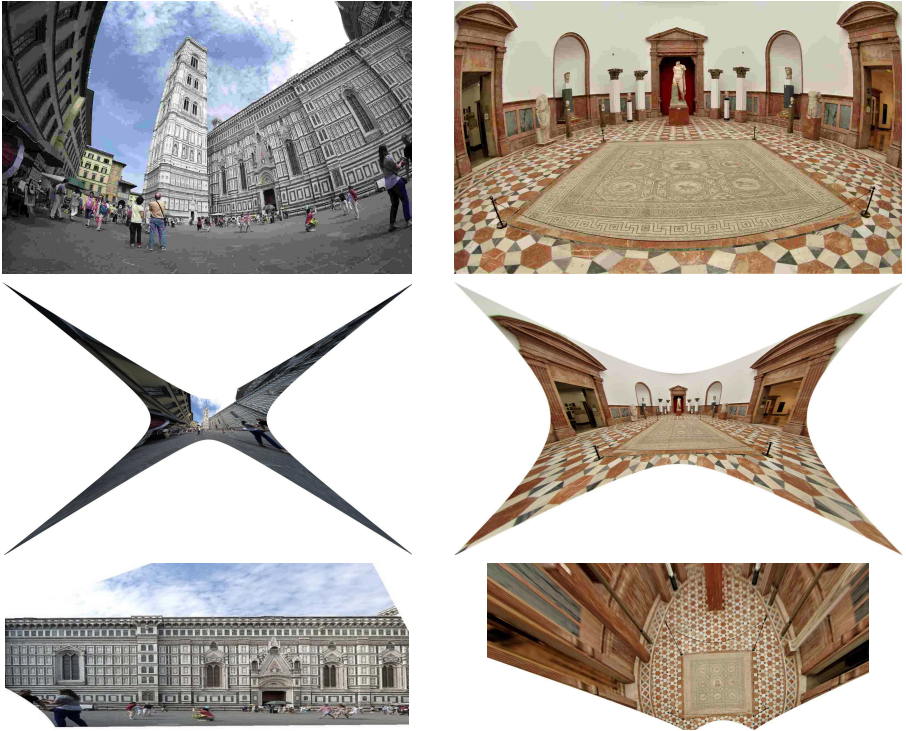


**Fig. C.3.** *Very wide-angle lenses.* The proposed method is tested on imagery taken 8mm and 10mm fisheye lenses. The division model used by [7] for radial lens distortion has only 1 parameter, which limits its use for modeling extreme lens distortion. Even so, the proposed method gives reasonable solutions for affine rectification and undistortion on very wide-angle lenses. Rectification quality is also dependent on the coverage of the features extracted. (top row) Input images (middle row) Undistorted images using  $H_{222}1\lambda + LO$  (bottom row) Undistorted and rectified results.

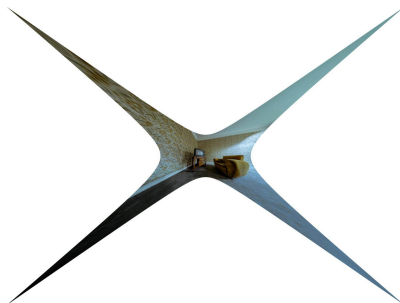


**Fig. C.4.** *Very wide-angle cameras.* The proposed method is tested on imagery taken from a 7.5mm fisheye lens. Some radial distortion is still visible in the undistorted image in the left column, perhaps due to sparse extracted features. (top row) Input images (middle row) Undistorted images using  $H_{222}1\lambda + LO$  (bottom row) Undistorted and rectified results.



**Fig. C.5.** *Very wide-angle cameras.* The proposed method is tested on imagery taken with more fisheye lenses. Some radial distortion is still visible in the undistorted image in the left column, perhaps due to the fact that the estimation was from measurements from the texture near the center of distortion. (top row) Input images: (left) 8mm lens, (right) 12mm lens. (middle row) Undistorted images using  $H_{222}1\lambda + LO$  (bottom row) Undistorted and rectified results.